



# CHORUS

This is the accepted manuscript made available via CHORUS. The article has been published as:

## Imaging and controlling vortex dynamics in mesoscopic superconductor-normal-metal-superconductor arrays

Tyler R. Naibert, Hryhoriy Polshyn, Rita Garrido-Menacho, Malcolm Durkin, Brian Wolin, Victor Chua, Ian Mondragon-Shem, Taylor Hughes, Nadya Mason, and Raffi Budakian

Phys. Rev. B **103**, 224526 — Published 24 June 2021

DOI: [10.1103/PhysRevB.103.224526](https://doi.org/10.1103/PhysRevB.103.224526)

1 **Imaging and Controlling Vortex Dynamics in Mesoscopic Superconductor-Normal-Superconductor**  
2 **Arrays**

3 Tyler R. Naibert<sup>1</sup>, Hryhoriy Polshyn<sup>1,2</sup>, Rita Garrido-Menacho<sup>1</sup>, Malcolm Durkin<sup>1</sup>, Brian Wolin<sup>1</sup>, Victor  
4 Chua<sup>1</sup>, Ian Mondragon-Shem<sup>1</sup>, Taylor Hughes<sup>1</sup>, Nadya Mason<sup>1,\*</sup>, and Raffi Budakian<sup>1,3,\*</sup>

5 <sup>1</sup>Department of Physics, University of Illinois at Urbana Champaign, 1110 W. Green St., Urbana, IL  
6 61801-3080, USA

7 <sup>2</sup>Department of Physics, University of California, Santa Barbara, CA 93106, USA

8 <sup>3</sup>Institute for Quantum Computing, University of Waterloo, Waterloo, ON, Canada, N2L3G1

9 Department of Physics, University of Waterloo, Waterloo, ON, Canada, N2L3G1

10 Perimeter Institute for Theoretical Physics, Waterloo, ON, Canada, N2L2Y5

11 Canadian Institute for Advanced Research, Toronto, ON, Canada, M5G1Z8

12 \*Corresponding authors. Email: [rbudakian@uwaterloo.ca](mailto:rbudakian@uwaterloo.ca); [nadya@illinois.edu](mailto:nadya@illinois.edu)

13  
14 Harnessing the properties of vortices in superconductors is crucial for fundamental science and  
15 technological applications; thus, it has been an ongoing goal to locally probe and control vortices. Here, we  
16 use a scanning probe technique that enables studies of vortex dynamics in superconducting systems by  
17 leveraging the resonant behavior of a raster-scanned, magnetic-tipped cantilever. This experimental setup  
18 allows us to image and control vortices, as well as extract key energy scales of the vortex interactions.  
19 Applying this technique to lattices of superconductor island arrays on a metal, we obtain a variety of striking  
20 spatial patterns that encode information about the energy landscape for vortices in the system. We interpret  
21 these patterns in terms of local vortex dynamics and extract the relative strengths of the characteristic energy  
22 scales in the system, such as the vortex-magnetic field and vortex-vortex interaction strengths, as well as  
23 the vortex chemical potential. We also demonstrate that the relative strengths of the interactions can be  
24 tuned and show how these interactions shift with an applied bias. The high degree of tunability and local  
25 nature of such vortex imaging and control not only enable new understanding of vortex interactions, but  
26 also have potential applications in more complex systems such as those relevant to quantum computing.

27  
28 **I. INTRODUCTION**

29 Many electronic and magnetic properties of superconductors can be understood through study of the  
30 vortices present in the superconductor. Each vortex allows one flux quantum to penetrate the  
31 superconducting surface, allowing the bulk of the superconductor to remain in the superconducting state.  
32 When an electrical current is applied, vortices move transversely to the current, a dissipative process that  
33 removes the perfect electrical conductivity of the system. Forces that prevent motion of vortices, known as  
34 pinning forces, are desirable to prevent this dissipation, and to control the positions that vortices occupy.

35 Beyond enhancing superconductivity, it is desirable to control vortex positions to predict vortex paths, as  
36 well as the fields surrounding the superconductor. The demonstration of locally probed and manipulated  
37 vortices [1-14] is relevant to a variety of technological applications, including quantum computation [15,  
38 16].

39 In previous works, imaging techniques such as scanning SQUID microscopy [1-3, 17], Hall probe  
40 microscopy [18, 19], scanning tunneling microscopy [6, 20], NV center magnetometry [21, 22], and  
41 cantilever-based techniques [23-26] have played a central role in studies of vortex lattices and the internal  
42 structure of individual vortices. However, these studies focused on probing and manipulating individual  
43 vortices rather than capturing and controlling the dynamics of an entire vortex ensemble. This allowed  
44 determination of the pinning strength but not the other important energy scales such as vortex-vortex  
45 interaction strength. Yet determining vortex interactions is crucial for enabling predictive vortex  
46 manipulation and control for applications. In this article we use a technique that overcomes this  
47 obstacle: a method we term  $\Phi_0$ -Magnetic Force Microscopy ( $\Phi_0$ -MFM) [27, 28], which probes the dynamic  
48 motion of a small group of vortices (from 1 to  $\sim 12$ ) trapped in the magnetic field generated by the tip of a  
49 vertically-oriented cantilever. Here, we use this technique to determine the vortex number in a pinned vortex  
50 configuration, extract the relative vortex-vortex and vortex-field interactions strengths as well as the vortex  
51 chemical potential, and probe the response to an applied current bias.

52

## 53 **II. $\Phi_0$ -MAGNETIC FORCE MICROSCOPY OF VORTEX DYNAMICS IN** 54 **SUPERCONDUCTOR-NORMAL-SUPERCONDUCTOR ARRAYS**

55  $\Phi_0$ -MFM is demonstrated on triangular arrays of Nb islands deposited on Au films [Fig. 1(a)],  
56 which form a superconductor-normal metal-superconductor (SNS) array. A resistance vs. temperature  
57 measurement showing a superconducting transition for a representative array is shown in Fig. 1(c). In this  
58 figure,  $T_1$  represents the superconducting transition temperature of the Nb islands and  $T_2$  the temperature at  
59 which the Au film regions between the Nb islands – the interstitial regions – become superconducting [31]  
60 and strongly Type II in behavior. Vortices will preferentially stay close to the magnetic tip but avoid the  
61 Nb islands and thus reside in the interstitial regions, since these regions host a weaker superconducting  
62 condensate. As a result, the SNS array system of superconducting islands on top of normal metal films  
63 proves to be a controllable and tunable model for superconducting films having a periodic pinning potential  
64 for vortices [29–31].

65 Scanning measurements are performed below  $T_2$  using an ultra-soft micromachined Si cantilever,  
66 mounted in a pendulum configuration, with an  $\text{SmCo}_5$  magnetic tip shaped via focused ion beam [Fig. 1(b)].  
67 All MFM scans are taken below  $T_2$  to allow us to neglect vortex nucleation due to thermal fluctuations and  
68 assume that all phase windings and density suppressions in the superconducting order parameter are due to

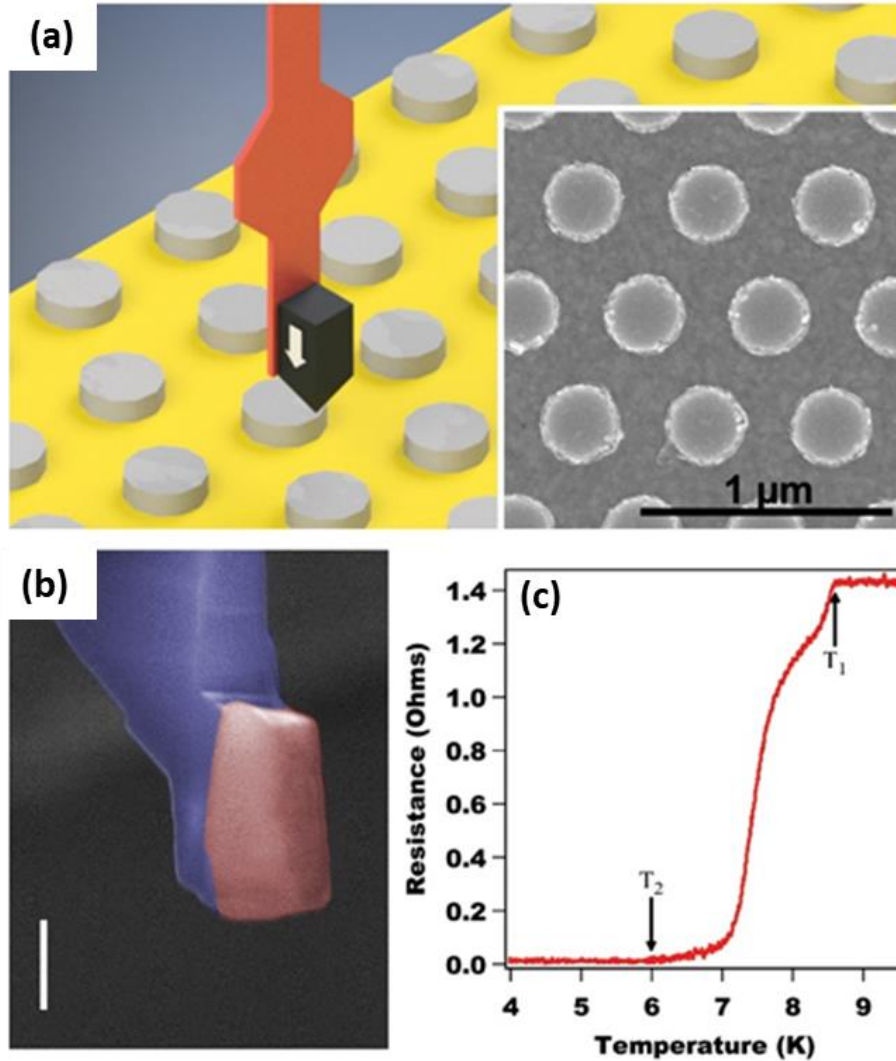


FIG. 1. SNS array and magnetic tip characterization. (a) Schematic of cantilever over a triangular array of Nb islands on top of an Au film. A SmCo<sub>5</sub> magnetic tip (black shape) is attached to the end of the cantilever and used to trap vortices. The white arrow on the magnetic tip indicates the direction of the tip's magnetization. Inset: Scanning electron microscope (SEM) image of an array with 500 nm center-to-center spacing. (b) False-color SEM image of one of the SmCo<sub>5</sub> magnetic tips used in this work. White scale bar is 500 nm. (c) Temperature dependence of the resistance near the superconducting transition.

69 external or tip magnetic fields. An estimate of the tip field is obtained by imaging flux entry into  
 70 superconducting Al rings (see Appendix A). A uniform magnetic field applied perpendicular to the SNS  
 71 array, and anti-parallel to the field of the tip, tunes the number of vortices trapped underneath the cantilever tip.  
 72 The magnetic tip creates a potential well underneath it for vortices with a particular circulation, and at the  
 73 same time, it repels oppositely circulating vortices that are generated by the uniform field applied to the  
 74 SNS array. Hence, underneath the tip several tip-induced vortices will be trapped. The tip field controls both  
 75 the depth and width of the well while the external applied field affects only the depth of the potential.

76 Overall, the external field serves as an additional tuning parameter which globally defines the vortex array  
 77 that is then modulated by the tip field. As parameters related to the vortex energies and interactions are  
 78 changed (e.g., tip height, magnetic field magnitude, array spacing) the configuration of the trapped vortices  
 79 changes to minimize the local energy. As the vortices move, frequency shifts of the cantilever are generated  
 80 due to the interaction between the vortex and cantilever fields.

81 To generate spatial frequency shift maps, the cantilever is raster scanned over the surface of the SNS  
 82 array at a fixed tip scanning height, with a small fixed oscillation amplitude (typically  $\sim 15$  nm), which  
 83 perturbs the position of the potential well that traps vortices [Fig. 2(a)-(e)]. The cantilever is kept oscillating

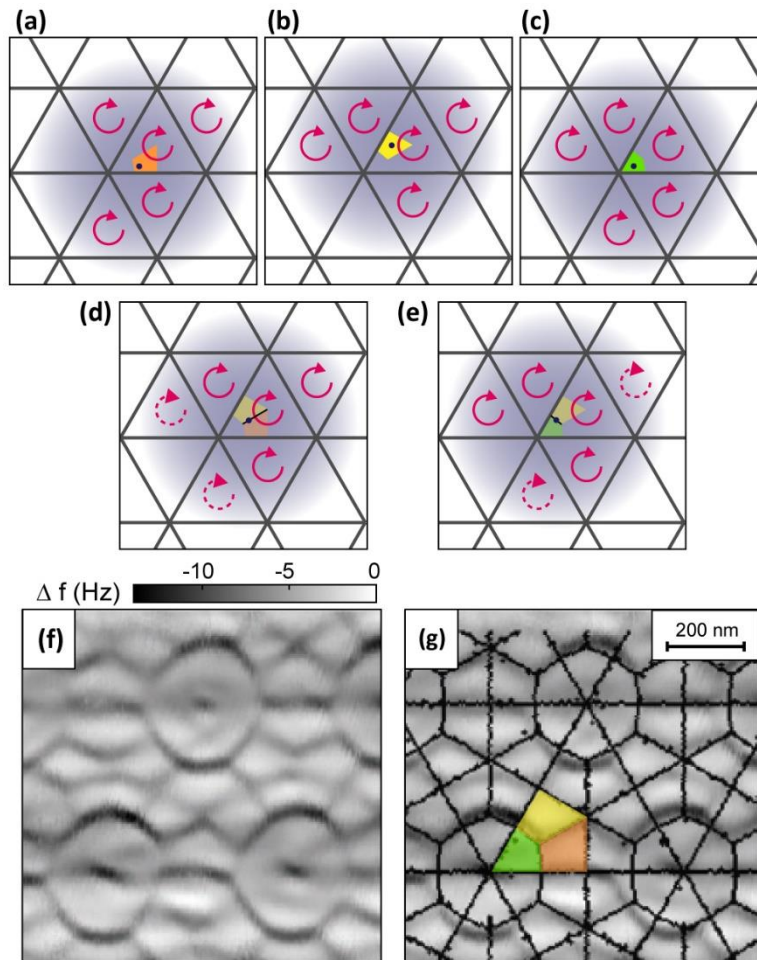


FIG. 2. Schematic showing formation of spatial frequency shift maps. (a)-(c) Several different vortex configurations are stabilized for different positions of the tip with respect to the island array. Here the vertices of triangles correspond to the positions of Nb islands and the shaded blue region marks the field on the surface of the sample with the center indicated by the dot. Vortices in the interstitial regions are shown by red circular arrows. Small colored regions mark the positions of the tip center for which the vortex configurations are stable. (d), (e) When the tip encounters a position where the vortex configuration changes (black line), it will drive the vortices between these configurations as it oscillates, leading to a force on the cantilever and the emergent resonant frequency shift. (f) Representative example of an experimental frequency shift. (g) Simulated locations of the transitions between vortex configurations overlaid with the experimental data. Shaded regions correspond to vortex configurations shown in (a)-(c).

84 at its resonant frequency [32] and is monitored by a phase-locked loop. When the cantilever moves across  
 85 the array at a fixed applied field the energies of two distinct configurations of vortices can become  
 86 degenerate at certain tip locations [Fig. 2(d), (e)]. While the cantilever is over these degeneracy locations,  
 87 the oscillations of the cantilever, along with thermal excitations of the vortices, will drive the vortices  
 88 between the two configurations in resonance with the cantilever, leading to a force on the cantilever and an  
 89 associated frequency shift. This frequency shift, which we found to be  $\Delta f \approx 5\text{-}15$  Hz for our cantilevers  
 90 with resonant frequency of  $f_0 \sim 4$  kHz, vanishes quickly as the cantilever moves away, sharply marking the  
 91 positions where the vortex configurations become degenerate. Raster scanning over the entire imaging  
 92 window leads to a spatial map of frequency shifts.

93 In Fig. 2(f) we present an experimental frequency shift map for an island spacing of 500 nm, where  
 94 dark lines indicate the boundaries between two stable vortex configurations and the lighter areas show tip  
 95 positions where the vortex configuration is stable and thus there is no associated frequency shift of the tip.  
 96 The figure shows an intricate pattern of approximately periodic frequency shifts. This pattern consist of a  
 97 series of nearly circular features, which are centered on the superconducting islands, and a series of lines,  
 98 some of which are horizontal, and others appear in zig-zag configuration. Once these spatial frequency shift  
 99 maps are obtained experimentally, we can infer the corresponding vortex configuration from Monte Carlo  
 100 simulations that minimize the energy of the system (see Section II.A). For example, our modelling indicates  
 101 that the frequency map shown in Fig. 2(f) corresponds to a 5-vortex configuration. Figure 2(g) shows the  
 102 comparison of the experimentally observed pattern with the calculated locations of transitions between  
 103 configurations of 5 vortices.

104

### 105 **A. Numerical simulations of vortex configurations**

106 To understand the underlying mechanism that causes the formation of these patterns, we will now discuss how  
 107 these images encode information about vortex dynamics in the SNS array. We performed numerical  
 108 simulations of a simple phenomenological model of vortices. We model the system as an array of Josephson  
 109 junctions, approximating the Josephson current as  $I \approx I_c \gamma_{ij}$ , where  $\gamma_{ij}$  is the gauge-invariant phase  
 110 between islands  $i$  and  $j$ . This approximation allows for several convenient simplifications to the effective  
 111 vortex energy (see Appendix B). We assume that each vortex is point-like and sits in the center of a  
 112 plaquette, and the subsequent model for the vortex energy is

$$E[n] = p_{\text{int}} \sum_{p,q=1}^{N_{\text{plaq}}} V_{pq} n_p n_q + \sum_{p=1}^{N_{\text{plaq}}} [(U_f)_p + \mu_{\text{vort}}] n_p \quad (1)$$

113 where  $N_{\text{plaq}}$  is the number of plaquettes,  $p_{\text{int}}$  is a relative scale factor between the vortex-field  $((U_f)_p)$   
 114 energy and vortex-vortex  $(V_{pq})$  interaction term,  $\mu_{\text{vort}}$  represents the chemical potential of the vortices,

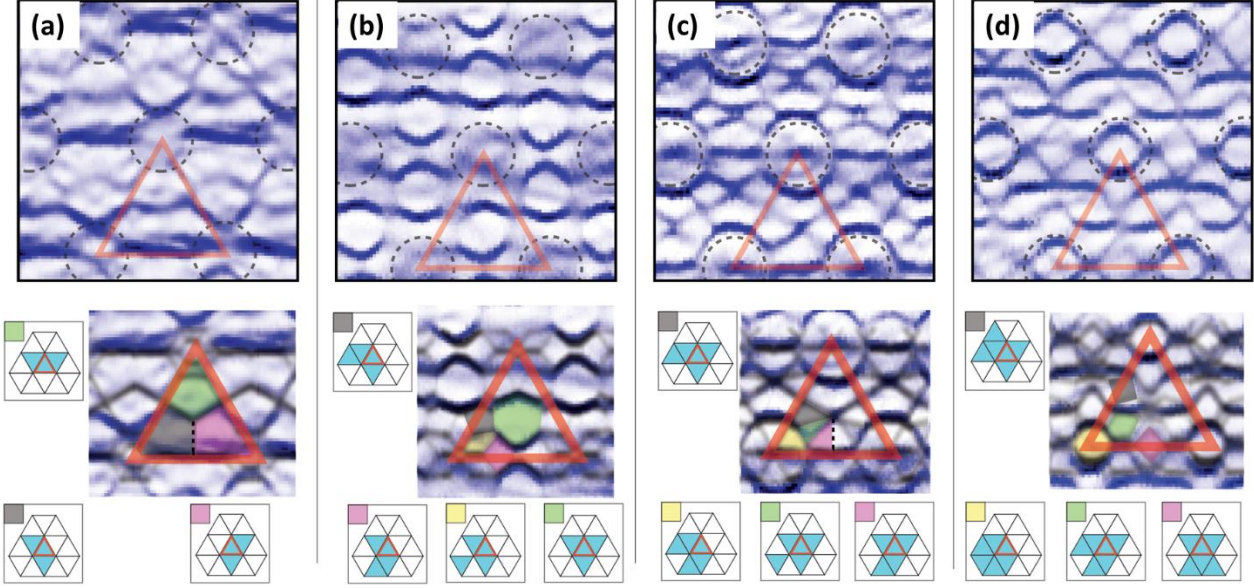


FIG. 3. Images of some patterns seen in this experiment (top) and associated vortex configurations (bottom) as determined by simulated annealing. A slowly varying background was removed from all images to highlight the pertinent features. Configurations are shaded where they are the lowest energy state. The simulation data is darker in areas where the cantilever would experience a larger frequency shift due to the oscillating current. Some dashed vertical lines are added to the simulation to highlight stable regions for a given vortex configuration. One plaquette (red triangle) and associated islands (dashed circles) are drawn for clarity. Experimental and simulations taken for (a) 3 (124 Oe, 350 nm), (b) 4 (85 Oe, 425 nm), (c) 5 (80 Oe, 425 nm), and (d) 6 vortices (68 Oe, 425 nm). All images taken at 3.70 K, except (B), taken at 3.75 K.

115 and  $n_p$  is the number of vortices in plaquette  $p$ . We use a classical Metropolis algorithm Monte Carlo  
 116 simulation to determine the lowest energy vortex configuration for a fixed vortex number (Appendix B). We  
 117 then compared the lowest energy vortex configurations for differing vortex numbers to determine the  
 118 configuration with the lowest overall energy, hence identifying the vortex number and its configuration for  
 119 a given tip location. By tuning the relative strengths of  $(U_f)_p$ ,  $V_{pq}$ , and  $\mu_{\text{vort}}$ , to fit the data at the correct  
 120 external field and tip heights, we can extract the relative energy scales of the system.

121 As an example of these simulations, in Fig. 3(a) we show the patterns and associated vortex  
 122 configurations produced by three vortices. As can be seen, there is very good agreement between the  
 123 simulations obtained from the model we use (bottom) and the experimental measurement (top). By  
 124 increasing the number of vortices by one and running the simulation again, the resulting pattern obtained  
 125 changes and reproduces another of the experimental scans, as shown in Fig. 3(b). Using this technique, we  
 126 can thus show that Figs. 3(a), (b), (c), and (d) demonstrate the energy landscapes and corresponding vortex  
 127 configurations for 3, 4, 5, and 6 vortices, respectively.

128

129

### B. Effects of tip scanning height and applied magnetic field

130

Figures 4 and 5 show additional real space maps of the frequency shifts associated with changes in

131 vortex configurations, where striking geometric patterns are produced as the applied field, tip height and  
 132 array spacing are tuned. Changes in the number of vortices and their energy landscapes are manifested as a  
 133 remarkable evolution between frequency shift patterns. We can controllably alter the number of vortices  
 134 and thus vortex configurations by tuning three main parameters: the applied magnetic field, tip scanning  
 135 height, and array spacing.

136 Figure 4(a)-(e) show frequency shift maps for a 500 nm-spaced island array obtained by fixing the  
 137 applied magnetic field to 50 Oe and tuning the tip height from 540 nm to 340 nm. Through Monte Carlo  
 138 simulations, it was determined that Fig. 4(a)-(e) correspond to a 3, 4, 5, 6, 7-vortex configuration,  
 139 respectively. As the tip scanning height is decreased at a fixed applied field, the depth of the potential well  
 140 increases, leading to an increase in the number of vortices trapped underneath the tip. Correspondingly, the  
 141 energy landscape evolves as the vortex number increases.

142 The tip heights at which a vortex configuration transition happens (for example a transition from a  
 143 3-vortex to a 4-vortex configuration) also depends on the applied magnetic field. Fig. 4(f)-(j) show  
 144 frequency shift maps obtained by fixing the applied field to a higher value of 80 Oe and tuning the tip height  
 145 from 380 nm to 240 nm. Similar features are evident in Fig. 4(a)-(e) and Fig. 4(f)-(j); from simulation, it  
 146 was determined that Fig. 4(f)-(j) also correspond to a 3, 4, 5, 6, 7-vortex configuration. However, for the  
 147 larger applied field the depth of the potential well trapping the tip-generated vortices is smaller and thus  
 148 there are fewer trapped vortices. For example, by fixing the tip height to 380 nm and tuning the magnetic

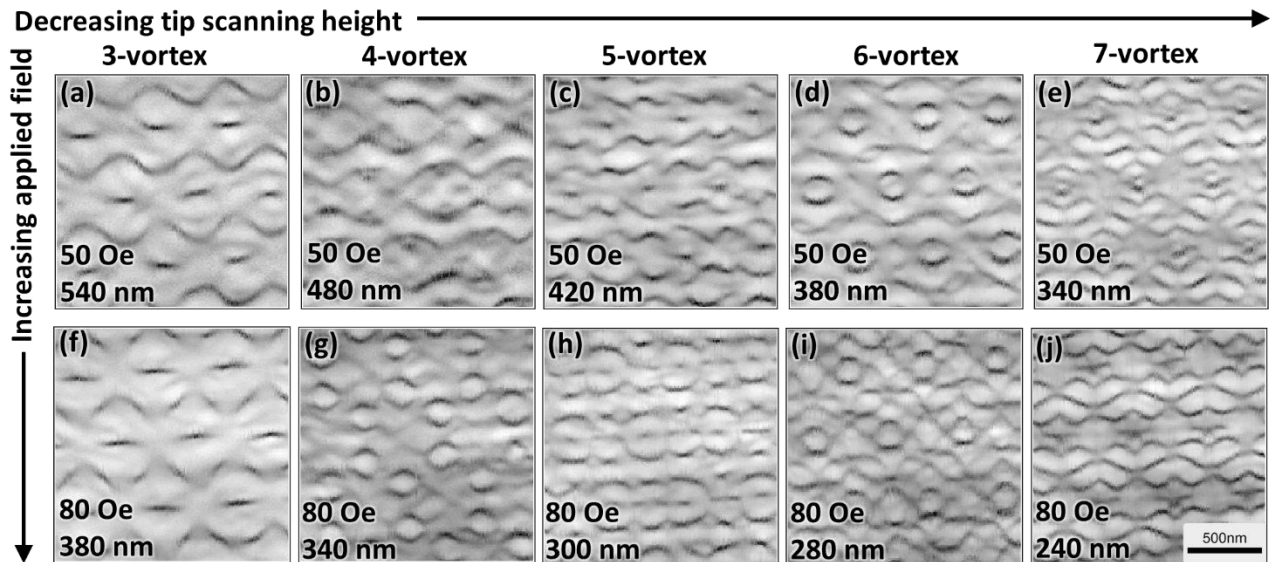


FIG. 4. Vortex configuration changes with tip height and applied magnetic field. Tip height decreases from left to right and applied field increases from top to bottom. The applied field (in Oe) and the tip height (in nm) are indicated on the lower left corner of each panel. (a-e) Applied field is fixed at 50 Oe as the tip height is tuned from 540 to 340 nm. As the tip height decreases, frequency shift maps were taken for (a) 3, (b) 4, (c) 5, (d) 6, and (e) 7 vortices. (f-j) Applied field is increased and fixed at 80 Oe as the tip height is tuned from 380 to 240 nm. As the tip height decreases, frequency shift maps were again taken for (f) 3, (g) 4, (h) 5, (i) 6, and (j) 7 vortices.



149 field from 50 Oe to 80 Oe, as shown in Fig. 4(d) and Fig. 4(f), the number of trapped vortices decreases  
150 from 6 to 3. It is clear that as the applied field increases, lower tip heights are required to achieve the same  
151 vortex configuration.

152 Although the frequency shift maps corresponding to the same vortex configurations are similar,  
153 they are not identical. For example, both Fig. 4(d) and Fig. 4(i) describe a 6-vortex configuration, however,  
154 they differ in that Fig. 4(i) has more well-defined features and also shows additional features not evident in  
155 Fig. 4(d). The differences in the patterns arise from a competition between vortex-tip and vortex-vortex  
156 interactions. With the tip closer to the surface of the array, vortex-tip interactions dominate, and the vortices  
157 are positioned in neighboring plaquettes. At higher tip heights, vortex-vortex interactions begin to  
158 dominate, and the vortices will begin to spread out underneath the tip and thus no longer reside in  
159 neighboring plaquettes (see Discussion for further details).

160 Altogether, the tip height and applied field will determine the number and energy landscape of  
161 trapped vortices, while the tip position affects the location of the vortices within that configuration. This  
162 shows that by constructing an appropriate field profile from the tip, control over the vortex states and  
163 extraction of key energy scales can be achieved. Using the model described in Section IIA, we can indeed  
164 infer the interaction energy scales by mapping the experimentally obtained images with our simulations.

165

### 166 **C. Effects of array spacing**

167 As the array spacing is tuned, control over the distribution of vortices can also be achieved. In  
168 addition to the 500 nm-spaced array discussed in Figs. 2 and 4, we measured arrays with a spacing of  
169 440 nm and 560 nm. Fig. 5(a)-(c) show frequency shift maps of a 6-vortex configuration for each array  
170 spacing at approximately the same tip scanning height. The frequency shift map for the closest-packed array  
171 with a 440 nm spacing [Fig. 5(a)] was taken at a tip height of 480 nm, an applied field of 35 Oe, and at a  
172 temperature of 7.7 K. The frequency shift map for the 500 nm array [Fig. 5(b)] was taken at a tip height of  
173 440 nm, an applied field of 40 Oe, and a temperature of 5.7 K. Lastly, the frequency shift for the 560 nm  
174 array [Fig. 5(c)] was taken at a tip height of 440 nm, an applied field of 65 Oe, and at a temperature of  
175 3.85 K. Measurements were made at different temperatures to ensure that all scans were taken at  
176 temperatures which are slightly below  $T_2$  [Fig. 1(c)]. The  $T_2$  value depends on the array spacing [31] where  
177 the smaller the array spacing, the larger the value of  $T_2$  up to the saturation value of bulk Nb  $T_c$ ; thus the  
178 frequency shift maps were taken at the appropriate temperatures right below  $T_2$ , with the 440 nm array  
179 having the largest temperature value and the 560 nm array having the smallest temperature value.

180 The magnitude of the applied field needed to create a vortex also depends on the array spacing  
181 through the magnetic frustration  $f = \frac{BA}{\Phi_0}$ , where  $B$  is the applied field,  $A$  is the plaquette area and  $\Phi_0$  is the  
182 flux quantum. As the plaquette area (proportional to the array spacing) decreases, the field needed to create

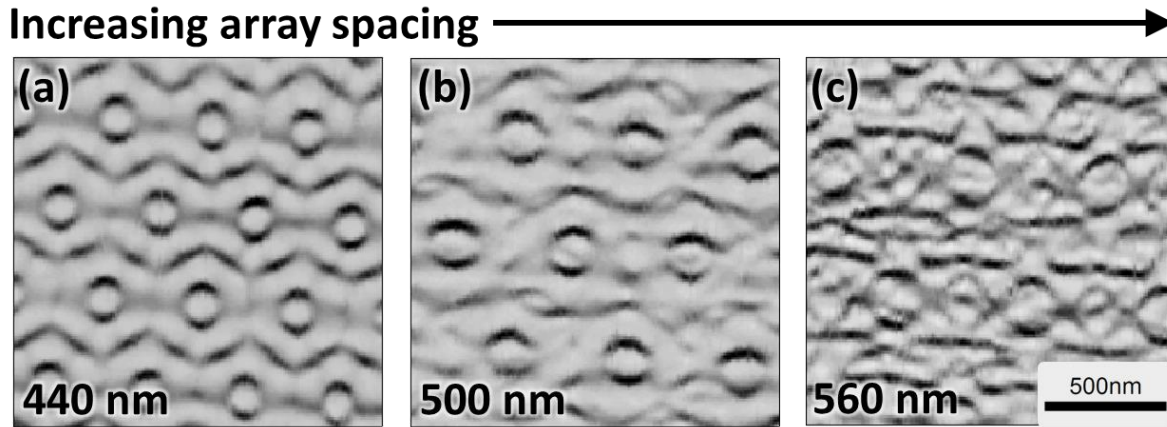


FIG. 5. Vortex pattern changes as a function of array spacing. 6-vortex configuration patterns at a tip height of approximately 480 nm for an array spacing of (a) 440 nm, (b) 500 nm, and (c) 560 nm.

183 a vortex in every plaquette ( $f = 1$ ) increases. Since the applied field is *anti-parallel* to the tip-field, the  
 184 relation between applied field and number of trapped vortices underneath the tip is reversed – the smallest  
 185 array spacing requires a smaller applied field to produce the same 6-vortex configuration as the largest array  
 186 spacing in Fig. 5.

187 It can be seen in Fig. 5(a)-(c) that there are similarities in the patterns, but they are not identical  
 188 even though they all represent the energy landscape of 6 vortices. These differences again arise due to  
 189 vortex-vortex interactions in the system. As the array spacing decreases, the tip field encompasses more  
 190 plaquettes, enabling the vortex-vortex interaction to spread out the vortices. Overall, the array spacing  
 191 serves as an additional tuning parameter; as we show in the Discussion, this allows for the extraction of the  
 192 relative strength of vortex-vortex and vortex-field interactions, which depend on whether the islands are  
 193 either loosely or closely-packed.

194

#### 195 **D. Effects of applied DC driving current**

196 We applied a DC current to the SNS arrays and again performed  $\Phi_0$ -MFM scans. The application of  
 197 a DC current results in a spatial shift of the frequency maps perpendicular to the current direction. Fig. 6(a)-  
 198 (c) show frequency maps for a 6-vortex configuration at a tip height of 270 nm for an applied DC driving  
 199 current of -35, 5 and 35  $\mu\text{A}$ , respectively. We find that the pattern shown in 6(a)-(c) shifts to the left by  
 200 about 55 nm as the applied current increases from -35 to +35  $\mu\text{A}$ ; the red circles are fixed guides added to  
 201 emphasize the relative shift of the patterns. We attribute this spatial shift to the Lorentz force acting on the  
 202 vortices as the current is applied. Fig. 6(d) shows the relation between the applied current and measured  
 203 spatial shift of the frequency maps for the 500 nm array when the vortex number and tip height is tuned.  
 204 The shift is determined from the calculated cross-correlation between two images taken with DC currents  
 205 of opposite directions (see Fig. 6(d) inset).

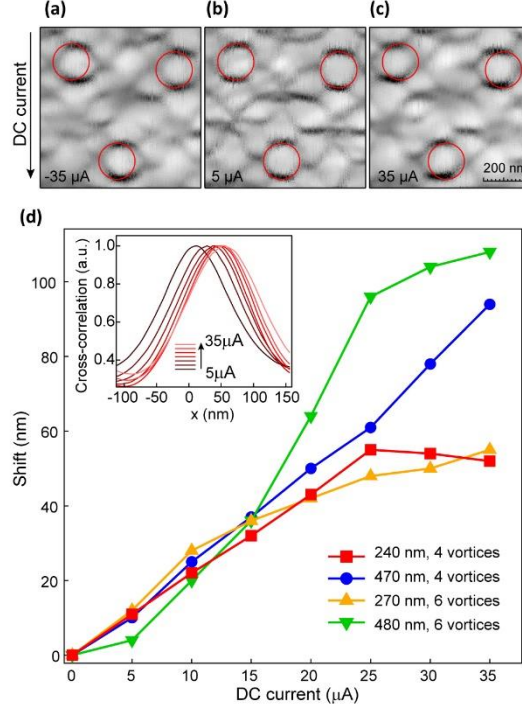


FIG. 6. Frequency maps as a function of an applied DC current. 6-vortex configuration at a tip height of 270 nm with an applied DC current bias of (a)  $-35 \mu\text{A}$ , (b)  $5 \mu\text{A}$ , and (c)  $35 \mu\text{A}$ . The red circles are fixed guides added to emphasize the relative shift of the patterns. (d) Spatial shift (in nm) of the frequency maps vs. the applied DC current for a 500 nm array spacing with a 4 and 6-vortex configuration at tip scanning heights of approximately 250 nm and 470 nm. Inset shows the cross-correlation curves used to determine the relative shifts between the images taken for 6-vortex configurations at 270 nm height.

206 We find that for low applied currents ( $I < 20 \mu\text{A}$ ) the pattern shift is approximately proportional to  
 207 the current (Fig. 6(d)). Remarkably, the corresponding coefficient does not show noticeable dependence on  
 208 the number of vortices or the height of the tip controlling the shape of the confining potential. This behavior  
 209 suggests that the pinning force, which is a linear restoring force arising when each vortex is shifted from  
 210 the center of its interstitial region [33], counteracts the Lorentz force due to the transport current. Since the  
 211 Lorentz force acting on each vortex is  $\mathbf{F} = \mathbf{J} \times \mathbf{z} \cdot \Phi_0$  [29], where  $\mathbf{J}$  is current density,  $\mathbf{z}$  is a unit vector  
 212 aligned with the vortex, and  $\Phi_0$  is the superconducting flux quantum, we find that the effective spring  
 213 constant in the linear regime is  $k \approx 1.6 \times 10^{-8} \text{ N/m}$ . It is worth pointing out that the spring constant  
 214 depends on the relative strength of  $\mathbf{J}$  and intrinsic supercurrents flowing between the islands which are of  
 215 the order of  $I_c$ . Therefore the measurement of  $k$  opens a pathway towards extracting the absolute values of  
 216 vortex energy scales. Such analysis, however, goes beyond the scope of this work and will require  
 217 calculation of vortex energy with a more realistic model which takes into account the distribution of currents  
 218 within plaquette and other factors.

219 In a 4-vortex configuration with a tip height of 470 nm, the shift increases linearly up to the  
 220 maximum applied current, however at tip height of 240 nm the linear behavior persists only up to about

221 25  $\mu\text{A}$  [Fig. 6(d)]. At higher currents the shift is independent of the applied current signaling a crossover to  
222 a regime in which vortex-vortex and vortex-field interactions likely dominate over the pinning force. The  
223 effect of decreasing the tip height while keeping number of vortices constant means that the tip field lines  
224 are now confined to fewer plaquettes on the array. This confinement coupled with large driving currents  
225 leads to the increased vortex-vortex and vortex-field interactions.

226 In a 6-vortex configuration at similar scanning heights of 270 nm and 480 nm [yellow and green  
227 traces in Fig. 6(d), respectively], the crossover to dominant vortex-vortex and vortex-field interactions  
228 happens at lower driving currents when compared to the 4-vortex configuration. More vortices confined  
229 over the same number of plaquettes on the array will be more susceptible to crossover to a vortex-vortex  
230 and/or vortex-field interaction regime at lower driving currents.

231 At even higher applied currents, when the Lorentz force dominates over the pinning force, vortex-  
232 vortex and vortex-field interactions lead to bulk depinning of the vortices. Once the vortices de-pin from  
233 their potential wells, the tip no longer detects frequency shifts and the image is smeared (see Appendix C).

234

235

### III. DISCUSSION

236 We fit patterns at different external fields and tip heights to extract valuable, and previously  
237 inaccessible, information about the energy scales that determine vortex dynamics in these systems. Using  
238 Eqn. (1), we find that, for a 500 nm center-to-center (inter-island) array, the chemical potential term is  
239 approximately  $\mu_{\text{vort}} = (1.8 \pm 0.1) V_{pp}$ , where  $V_{pp}$  is the energy of a lone vortex trapped in the array with no  
240 fields applied, as presented in the model described in Appendix B, and  $p_{\text{int}}$  is approximately 1.0–1.2. We do  
241 not find any dependence of  $\mu_{\text{vort}}$  on the number of vortices underneath the tip for the configurations examined.  
242 Separate arrays with spacings of 440 and 560 nm were also imaged, and  $\mu_{\text{vort}}$  and  $p_{\text{int}}$  were extracted. For the  
243 560 nm array, we found  $\mu_{\text{vort}} = (0.9 \pm 0.1) V_{pp}$ , with  $p_{\text{int}} \sim 0.7 - 0.9$ , i.e., showing vortex-vortex interactions  
244 are weaker relative to vortex-field interactions. We also find that  $p_{\text{int}}$  depends on the external field and  
245 decreases for higher external magnetic field values. The 440 nm array has  $\mu_{\text{vort}} = (2.4 \pm 0.1) V_{pp}$ , with  $p_{\text{int}}$   
246  $\sim 1.2 - 1.4$ , indicating stronger vortex-vortex interactions relative to the vortex-field interaction. For this  
247 lattice spacing we find that  $p_{\text{int}}$  increases for higher field values.

248 In addition to the extraction of these characteristic energy scales, some in-situ control over the  
249 vortex configurations is achieved by varying the height of the tip as previously discussed. By simulating  
250 the effects of the tip height on a certain vortex configuration, we were able to further extract the location of  
251 each vortex within the array. Fig. 7 shows the evolution of configurations of 6 vortices and accompanying  
252 simulations as the tip height is increased and the applied field is tuned so to keep the number of vortices  
253 constant. At a tip height of 430 nm, it was demonstrated by the simulation that the vortices reside in  
254 neighboring plaquettes (Fig. 7). As the tip height is increased, the vortices begin to spread out and begin to

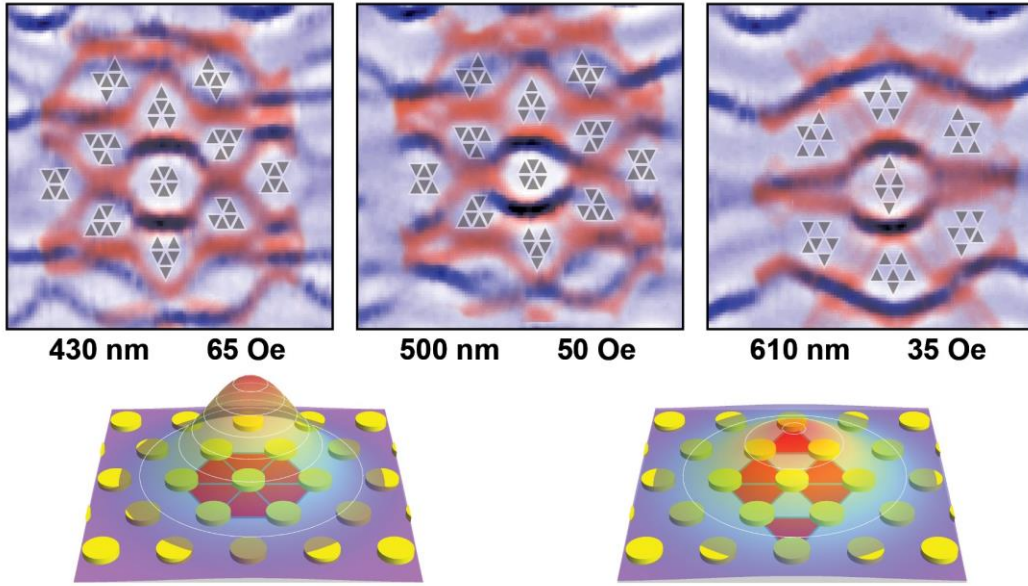


FIG. 7. Simulated vortex pattern changes with height for 6 vortices underneath the tip. Tip height increases from left to right, as shown below each image. Images are overlaid with data from simulations (red) and the stable vortex configuration in each region. As the tip height is increased, the potential well flattens out, while the associated external field is changed to keep the number of vortices constant. Some stable vortex configurations cover a smaller area as the tip height is increased, with those regions disappearing in the furthest image. In the rightmost image,  $\mu_{\text{vort}}$  was decreased to  $1.4V_{\text{pp}}$  to achieve a better fit. The lower images show the field distribution on the surface for 430 nm (left) and 610 nm (right) tip separations with the tip over the central feature of the top images.

255 reside in next-nearest neighboring plaquettes. Some vortex configurations that are present with a deeper  
 256 well will cover less area in the image or can even disappear as the well is made shallower. This again is due  
 257 to the vortex-vortex interactions becoming relatively stronger, and hence more significant in determining  
 258 the vortex configurations for these conditions.

#### 259 IV. CONCLUSIONS

260 In conclusion, we have demonstrated a robust experimental platform for locally probing and  
 261 controlling vortex dynamics. By trapping vortices underneath a magnetic tip, we can characterize transitions  
 262 between stable vortex configurations and are able to extract the relative energy scales of various  
 263 interactions. We tune the number and distribution of vortices trapped underneath the tip by modifying the  
 264 scan height, external field, and array spacing. Using simulations of a simple model of vortices, we can  
 265 reproduce the observed image patterns. The versatility of this experimental platform could prove a powerful  
 266 tool to obtain a local understanding of, for example, the dominant effects that lead to various forms of vortex  
 267 matter in superconductors such as vortex glasses and vortex liquids. We note that this technique is useful  
 268 for mapping and manipulating vortex configurations even in systems without periodic pinning  
 269 potentials. Furthermore, this technique has the potential of probing non-standard vortex interactions in

270 novel superconducting systems. In particular, these results open interesting opportunities for applications  
271 in quantum computing platforms that require the manipulation and braiding of vortices.

272

273

## ACKNOWLEDGEMENTS

274 This work was supported by the DOE Basic Energy Sciences under DE-SC0012649 and the National  
275 Science Foundation (NSF) under DMR 17-10437. V.C. was supported by the Gordon and Betty Moore  
276 Foundation EPiQS Initiative through Grant GBMF4305. NM also acknowledges support from DOE-EFRC  
277 under DE-SC0021238 for analysis/manuscript preparation. This research was carried out in part in the  
278 Frederick Seitz Materials Research Laboratory Central Research Facilities, University of Illinois.

279

280

## APPENDIX A: MATERIALS AND METHODS

281

### 1. Device Fabrication

282

283

284

285

286

287

288

289

290

291

292

Electron beam lithography and electron beam evaporation were used to define and deposit several layers of material. The first, an 18 nm Au layer, with an underlying 1 nm Ti adhesion layer was placed onto a Si substrate with 300 nm SiO<sub>2</sub> as an insulator. The second layer consists of Al registration marks to aid in determining the location of the tip on the surface. A final round of processing was used to define and deposit the Nb islands. Prior to the Nb deposition, the surface of the Au was Ar<sup>+</sup> ion milled to establish a clean interface, and the Nb was evaporated at a pressure of  $\sim 10^{-9}$  Torr. For one sample, one 500 nm center-to-center spaced array was made on an Au pad of  $80 \mu\text{m} \times 80 \mu\text{m}$ . For the second sample, two 500 nm spaced arrays were  $50 \mu\text{m} \times 50 \mu\text{m}$ , with one connected in a four-point configuration. The connected array was used to determine the transition temperatures [Fig. 1(c)] and the magnetoresistance of the 500 nm spaced arrays, while the other was used for imaging experiments. Further arrays on the same sample, with lattice spacings of 440, 500, and 560 nm were also imaged. These arrays had areas of  $50 \mu\text{m} \times 15 \mu\text{m}$ .

293

294

295

296

297

298

299

The cantilevers used in this work were custom-fabricated Si cantilevers of length  $110 \mu\text{m}$ , width  $4 \mu\text{m}$ , and thickness 100 nm. A SmCo<sub>5</sub> magnetic particle was positioned on the end of each cantilever using a micromanipulator, aligned with the cantilever axis using an external magnet, then epoxied into position. The magnet was then shaped using a Ga focused ion beam with low ( $< 10$  pA) current to preserve the magnetization of the SmCo<sub>5</sub>. Torque cantilever magnetometry was used to measure the magnetic moment of the tip and ensure that it is well aligned with the cantilever axis.

300

### 2. Measurement

301

302

303

Measurements were taken in a He-3 refrigerator with a base temperature of 300 mK. Cantilever oscillations were measured using a laser interferometer, and the cantilever was self-oscillated using a feedback loop at a small amplitude, typically 15 nm. Frequency was determined using a phase-locked loop running on

304 an FPGA. Images were taken at least  $5\ \mu\text{m}$  from the edge of the arrays to minimize edge effects. Images  
305 were raster-scanned using an ANSxyz100 (Attocube) piezoelectric scanner, with the fast axis in the  $y$ -  
306 direction (vertical), at a rate of less than 300 nm/sec.

### 307 **3. Tip Field Estimate**

308 To estimate the tip field, the magnetic tip was scanned over superconducting Al rings deposited via  
309 e-beam or thermal evaporation. The rings used had radii of 2-5  $\mu\text{m}$ , with wall thicknesses of  $\sim 200\ \text{nm}$ .  
310 Sufficiently close to the superconducting transition, the fluxoid transitions in the ring become reversible and  
311 occur when the tip applies a half-integer number of magnetic flux quanta through the ring. The resulting  
312 strong interaction between the magnetic tip and the switching supercurrent shifts the resonant frequency of  
313 the cantilever [27, 28]. We mapped the locations of these frequency shifts as positions where the flux  
314 through the ring has changed by one flux quantum.

315 A model of the tip was then created consisting of  $50 \times 50 \times 50\ \text{nm}^3$  voxels with a magnetic dipole  
316 at the center. The tip magnetization was set to be the measured value, as determined by cantilever  
317 magnetometry. A scanning electron micrograph is used to determine where to position the dipoles, and their  
318 strength is adjusted to match the observed flux changes as the simulated tip is scanned across a ring. The  
319 dipoles are adjusted until the simulated flux changes and observed flux changes line up at multiple scan  
320 heights. Estimates of the tip field were then generated from the final dipole configuration. For a detailed  
321 description of this procedure for the tip field estimate refer to previous work in Ref. 27.

322

## 323 **APPENDIX B: VORTEX MODEL IN MONTE CARLO SIMULATIONS**

324 The simulated environment consisted of a roughly circular array of plaquettes 50 lattice constants in  
325 diameter. Vortices were placed and could move in the central 85 plaquettes of this larger area. Vortices  
326 were initialized dependent on the flux in each plaquette from the magnetic tip and external field. Vortex-  
327 antivortex pairs were randomly generated in the 85 plaquette area, and the new vortex configuration energy  
328 was compared to the previous state. The lowest energy state was selected using a simulated annealing  
329 procedure. The minimum energy states generated from this procedure for differing vortex numbers were then  
330 compared using the energy formula given in Eqn. (1), and the lowest energy state was selected for each tip  
331 position.

332

### **1. Josephson junction array model**

333 We start with a phenomenological model based on Josephson junction arrays. This amounts to neglecting  
334 the SC condensate in the interstitial regions altogether and focuses only on the Nb islands and their inter-  
335 island Josephson couplings. The interstitial regions, which host a weaker SC condensate, then act as  
336 Josephson weak links. Vortices that occupy the interstitial regions are essentially Josephson vortices in  
337 this picture. Thus we consider the following Josephson junction array quantum Hamiltonian [29, 31, 34]

$$\hat{H} = \frac{1}{2} \sum_{i,j} U_{ij} \hat{Q}_i \hat{Q}_j - \sum_{i \neq j} J_{ij} \cos(\hat{\theta}_i - \hat{\theta}_j - \varphi_{ij}[\mathbf{A}]) \quad (\text{A1})$$

338 where the  $i, j$  indices label the individual Nb islands. The operators  $\hat{Q}_i$  and  $\hat{\theta}_i$  refer to the charge  $2e$  Cooper  
 339 pair number, and SC phase operators respectively. They are mutually conjugate and satisfy the  
 340 commutation relation

$$[\hat{Q}_i, \hat{\theta}_j] = -i\delta_{ij} \quad (\text{A2})$$

341 The first term in  $\hat{H}$  is the charging energy with  $U_{ij}$  being proportional to the inverse of the capacitance  
 342 matrix. The second term is the Josephson coupling term with coupling matrix  $J_{ij}$  between sites  $i, j$ . The  
 343 quantity  $\varphi_{ij}[\mathbf{A}]$  is an additional phase term that originates from the presence of a magnetic vector  
 344 potential  $\mathbf{A}(\mathbf{x})$  associated to a non-zero out of plane magnetic field  $B_z$ . It ensures that the phase difference

$$\gamma_{ij} = \hat{\theta}_i - \hat{\theta}_j - \varphi_{ij}[\mathbf{A}] = -\gamma_{ji} \quad (\text{A3})$$

345 on the link between  $i$  and  $j$  is gauge invariant.

346 Next, we make three simplifying approximations:

- 347 1. The charging term, which is typically small for mesoscopically large SC islands, is discounted.  
 348 Effectively the Nb islands function as charge reservoirs (Cooper pair boxes) with large capacitances.  
 349 This turns  $H$  into a classical energy functional on the set of island phases  $\{\theta_i\}$ .
- 350 2. The Josephson couplings are limited to only nearest neighbors ( $ij$ ) of the triangular lattice island  
 351 array. This is rationalized by the fact that  $J_{ij}$  decays with increasing inter-island distance making  
 352 Cooper pair tunneling between nearest neighbors the dominant interaction. We expect that the  
 353 reincorporation of the neglected Josephson couplings will not qualitatively change main the results  
 354 of our analysis.
- 355 3. We assume that the value of the phase differences  $\gamma_{ij}$  are small, hence legitimizing a Taylor expansion  
 356 of the cosine. This is equivalent to assuming that the Josephson supercurrents  $I_{ij}$  between islands  $i$ ,  
 357  $j$  are small enough such that  $I_{ij} = I_c \sin(\gamma_{ij}) \approx I_c \gamma_{ij}$ , where  $I_c$  is the critical supercurrent between nearest  
 358 neighbors.

359 With these simplifications, the model is re-interpreted as a *static* Josephson junction array on a triangular  
 360 lattice with the Josephson supercurrents  $I_{ij}$  defined on nearest neighbor links ( $ij$ ), as the effective degrees  
 361 of freedom. This has the following effective static energy function

362

$$E_{\text{eff}}[I] = \frac{E_J}{2I_c^2} \sum_{\langle i,j \rangle} (I_{ij})^2 \quad (\text{A4})$$

363 where  $E_J$  is the Josephson energy between nearest neighbor SC islands and we have dropped an irrelevant



364 constant. It is convenient at this point to choose an orientation convention for the links ( $ij$ ) in organizing  
 365 the currents  $I_{ij}$ , and to avoid over-counting. A simple choice is to take a counter-clockwise orientation in  
 366 the up-pointing triangular plaquettes ( $\Delta$ ) which leads to a clock- wise orientation on the down-pointing  
 367 triangular plaquettes ( $\nabla$ ).

368 Magnetic flux penetrates the system through the triangular plaquettes of the lattice by an amount  
 369  $\Phi_{\text{ext}}[p]$  externally applied through plaquette  $p$ . In the absence of SC vortices,  $-\Phi_{\text{ext}}[p]$  is proportional  
 370 to the supercurrent density circulation  $\oint \mathbf{j} \cdot d\mathbf{l}$  enclosing plaquette  $p$  [29] within the Au film. This  
 371 supercurrent density circulation is proportional to the sum of phase differences which gives

$$-\Phi_{\text{ext}}[p] = \alpha \sum_{i,j \in p}^{\mathcal{U}} I_{ij} \approx \frac{\Phi_0}{2\pi} \sum_{i,j \in p}^{\mathcal{U}} \gamma_{ij}$$

372 where  $p$  is a label of the plaquette,  $\Phi_0 = h/2e$  is the flux quanta, and  $\alpha > 0$  is a proportionality constant  
 373 depending on geometry of the system, the magnetic permeability and the condensate density. The sums  
 374 are taken in the anti-clockwise ( $\mathcal{U}$ ) sense; for both  $\Delta$  and  $\nabla$  plaquettes. Note that the plaquettes themselves  
 375 reside in a honeycomb lattice dual to the triangular lattice.

376 Now, when a SC vortex is present in  $p$ , the sum of phase differences  $\gamma_{ij}$  is of order  $2\pi$  and is no longer  
 377 expected to be small such that the linear approximation  $\sin x \approx x$  (assumption 3. above) holds.  
 378 Nevertheless, we can perform a (large) gauge transformation which changes sum of phase differences by  
 379 quantized multiples of  $2\pi$  or fluxoids

$$\sum_{i,j \in p}^{\mathcal{U}} \gamma_{ij} \rightarrow \sum_{i,j \in p}^{\mathcal{U}} \gamma_{ij} \pmod{2\pi} = \sum_{i,j \in p}^{\mathcal{U}} \gamma_{ij} - 2\pi n_p$$

380 such that the  $\gamma_{ij}$ 's and hence their sum is small once more. Incorporating this into the relation with  
 381  $\Phi_{\text{ext}}[p]$  yields

$$\sum_{i,j \in p}^{\mathcal{U}} \gamma_{ij} = 2\pi n_p - \frac{2\pi \Phi_{\text{ext}}(p)}{\Phi_0}$$

382 where  $n_p \in \mathbb{Z}$  is an integer that is non-zero whenever a vortex (anti-vortex) is present in  $p$ . The external  
 383 flux is more conveniently expressed as

$$\Phi_{\text{ext}}(p) = \Phi_0 f_p \tag{A5}$$

384 with  $f_p$  being the local magnetic flux fraction or frustration at  $p$ . Thus we have the following constraint  
 385 equation for each plaquette

$$\frac{1}{I_0} \sum_{i,j \in p}^{\mathcal{U}} I_{ij} = n_p - f_p \tag{A6}$$

386 where  $I_0^{-1} \equiv \alpha/\Phi_0$  is a proportionality constant with dimensions of  $[\text{Current}]^{-1}$ . A second constraint on  $I_{ij}$

387 is current conservation, or Kirchoff's first law, at each site  $i$ . We express this as

$$\sum_{j \in (ij)}^{\odot(i)} I_{ij} = 0 \quad (\text{A7})$$

388 where the symbol  $\odot(i)$  denotes the fact that orientation convention of  $I_{ij}$  is chosen to be pointing *into*  
 389 the site  $i$ . These constraints must hold for all sites  $i$ . Implicit in these expressions is the neglect of the  
 390 mutual and self-inductance terms due to the supercurrents themselves which are generally expected to  
 391 be a small effect [30].

392

393

## 2. Counting Independent Currents

394

395

396

397

398

399

400

401

Now a unit cell of a triangular lattice has 1 site, 2 plaquettes and 3 links. Hence on average per site, current conservation (Eqn. (A7)) removes 1 independent current/link degree of freedom such that the flux conditions (Eqn. (A6)) relate 2 independent currents  $I_{ij}$  to 2 independent vortex numbers  $n_p$  given fixed frustrations  $f_p$ . In the case of a finite lattice with open boundaries, after a proper accounting of the links at the boundary, and noting that there are only  $(N_{\text{node}} - 1)$  current conservation constraints for  $N_{\text{node}}$  sites, we find a 1-1 relation between independent currents and a specified configuration of  $n_p$ 's on each plaquette. This reduction of the current conservation constraints by one comes from the fact that the entire system must have a net zero current.

402

403

404

405

406

407

This can also be seen by noting the Euler characteristic  $\chi = 1$  for a finite planar graph relates  $N_{\text{node}} - N_{\text{link}} + N_{\text{plaq}} = 1$  where  $N_{\text{node}}$  is the number of island sites,  $N_{\text{link}}$  is the number of nearest neighbor links, and  $N_{\text{plaq}}$  the number of triangular plaquettes. By rearranging we have  $N_{\text{plaq}} = N_{\text{link}} - (N_{\text{node}} - 1)$  which says that  $N_{\text{plaq}}$  is the same as the number of independent current links. Hence, for fixed frustrations  $\{f_p\}$ , specifying a configuration of vortex numbers  $n_p$  for all plaquettes is equivalent to specifying a current configuration  $I_{ij}$  on all links that obey the required constraints.

408

409

## 3. Transforming Currents to Vortex Occupations

410

411

412

By combining the constraints in equations (A6) and (A7), we can relate a configuration of vortex numbers  $\mathbf{n} = \{n_p\} \in Z^{N_{\text{plaq}}}$  to a configuration of currents  $\mathbf{I} = \{I_{ij}\} \in R^{N_{\text{link}}}$ . This relation is linear and can be succinctly expressed as

$$\frac{1}{I_0} \mathbf{M} \mathbf{I} = \begin{pmatrix} \mathbf{n} - \mathbf{f} \\ \mathbf{0}_{N_{\text{node}}-1} \end{pmatrix} \quad (\text{A8})$$

413

414

415

where  $\mathbf{f} = \{f_p\} \in R^{N_{\text{plaq}}}$  are the externally applied flux fractions/frustrations and  $\mathbf{0}_{N_{\text{node}}-1}$  is a  $(N_{\text{node}} - 1)$  dimensional zero vector. The matrix  $\mathbf{M}$  is  $N_{\text{link}} \times N_{\text{link}}$ , dimensionless and invertible due to the counting arguments just mentioned. Taking the inverse yields

$$\mathbf{I} = I_0 \mathbf{M}^{-1} \begin{pmatrix} \mathbf{n} - \mathbf{f} \\ \mathbf{0}_{N_{\text{node}}-1} \end{pmatrix} \quad (\text{A9})$$

416

417

#### 4. Effective Energy Function

418 Next, inserting the expression (9) into the effective energy function (4) gives

$$E_{\text{eff}}[\mathbf{n}, \mathbf{f}] = \frac{E_j}{2(I_c/I_0)^2} (\mathbf{n} - \mathbf{f})^T B^T B (\mathbf{n} - \mathbf{f}) \quad (\text{A10})$$

419

420

421

422

423

424

425

426

where  $B$  is a submatrix of  $\mathbf{M}^{-1}$  in its first  $N_{\text{plaq}}$  columns. The prefactor on the RHS sets the overall energy scale, and the dimensionless constant  $I_c/I_0$  encodes geometric information about the lattice. We consider the configuration of local frustrations  $\mathbf{f}$  to be a fixed external knob, and the vortex numbers  $\mathbf{n}$  as variational parameters that are required to minimize  $E_{\text{eff}}$ . The frustrations  $\mathbf{f}$  are determined by the total amount of flux through each plaquette, and are set by the  $B_z$  profile induced by the magnetic tip, and the additional uniform field that moderates the tip field. While calculating  $\mathbf{f}$  we ignored the redistribution of the magnetic flux due to field screening by Nb islands and inter-island supercurrents.

427

428

Then by scaling away the overall energy scale, expanding the brackets, and dropping an irrelevant constant we find the following model energy function dependent on  $\mathbf{n}$  and  $\mathbf{f}$

$$E[\mathbf{n}, \mathbf{f}] = \mathbf{n}^T \mathbf{V} \mathbf{n} + \mathbf{U}_f^T \mathbf{n} \quad (\text{A11})$$

429

where

$$\mathbf{V} = B^T B \quad (\text{A12})$$

$$\mathbf{U}_f = -2B^T B \mathbf{f} = -2\mathbf{V} \mathbf{f} \quad (\text{A13})$$

430

431

432

433

434

435

Note that  $E[\mathbf{n}, \mathbf{f}]$  is determined entirely by the geometry of the lattice and the local flux and current constraints. The first term in  $E[\mathbf{n}, \mathbf{f}]$  represents vortex-vortex interactions while the second is the vortex-field interaction. We note that the matrix  $\mathbf{V}$  is symmetric and is dense in its off-diagonals. This results in long-range, pair-wise interactions between vortices and externally applied fields. For our simulations we calculate the entries of  $\mathbf{V}$  for a roughly circular array of triangular plaquettes with a diameter of 50 lattice constants.

436

437

438

439

440

441

442

The entries in  $\mathbf{n}$  are integers, and due to the large number of possible combinations of vortex positions in  $\mathbf{n}$ , the minimization of  $E[\mathbf{n}, \mathbf{f}]$  is done variationally using Metropolis Monte-Carlo. In practice  $n_p$  takes 0, 1 values indicating the absence or presence of a single vortex. We simulate an area consisting of 85 plaquettes in a roughly circular region at the center of the larger, 50 lattice constant array to determine the vortex configurations. Also the total vortex number  $n_p$  is varied during the search for the energy minimum, but remains fixed during a single Monte-Carlo run. Since the number of vortices is small ( $n_p < 10$ ) we found that Metropolis Monte-Carlo is converging well to the ground state configuration

443 of vortices.

444  
445

## 5. Further Phenomenological Fitting

446 As it stands, there are no fitting parameters in the model, which itself depends heavily on all the  
447 assumptions previously discussed. However, to fit to the observed data, we have found it necessary to  
448 modify the above form of  $E[\mathbf{n}, \mathbf{f}]$ . The modified model energy function that we optimize is

$$E[\mathbf{n}, \mathbf{f}] = p_{\text{int}} \mathbf{n}^T \mathbf{V} \mathbf{n} + U_{\mathbf{f}}^T \mathbf{n} \quad (\text{A14})$$
$$+ \mu_{\text{vort}} \sum_p n_p = p_{\text{int}} \sum_{p,q=1}^{N_{\text{plaq}}} V_{pq} n_p n_q + \sum_{p=1}^{N_{\text{plaq}}} [(U_{\mathbf{f}})_p + \mu_{\text{vort}}] n_p$$

449 where  $p_{\text{int}}$  and  $\mu_{\text{vort}}$  are the two phenomenologically introduced parameters. The quantity  $p_{\text{int}}$  modulates  
450 the relative strength between vortex-vortex to vortex-field interactions. While  $\mu_{\text{vort}}$  is a chemical potential  
451 for the vortices that is added to fine-tune the favored number of vortices and adjusted so that vortex  
452 transitions occur at the observed field/heights in the experiment. These two fitting parameters can be  
453 thought of as modifications needed to compensate for the limitations of the assumptions and  
454 approximations made. For example, the fixed vortex number during a Monte-Carlo run excludes the  
455 possibility of fluctuating vortex numbers during a raster scan of the magnetic tip positions. In general,  $\mu$   
456 and  $p_{\text{int}}$  are not universal and depend on the parameters of the array that control the strength and  
457 geometry of supercurrents in system.

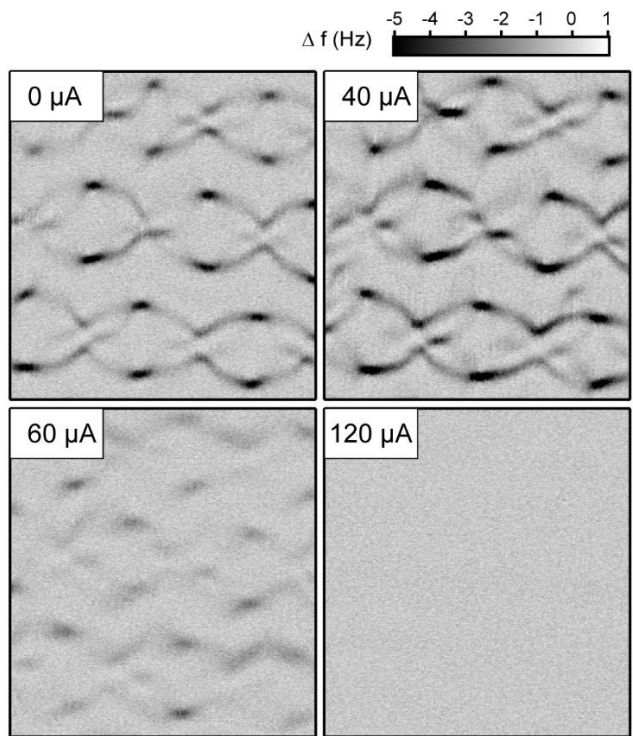
458 From fitting the data, we find the chemical potential  $\mu_{\text{vort}}$  of the 500 nm array, to be approximately  
459  $(1.8 \pm 0.1) \times V_{pp}$ , where  $V_{pp}$  is the on-site vortex energy. For the 440 nm and 560 nm arrays,  $\mu_{\text{vort}}$  is  
460 approximately  $(2.4 \pm 0.1) \times V_{pp}$  and  $(0.9 \pm 0.1) \times V_{pp}$ , respectively. In this case,  $p_{\text{int}}$  is approximately  
461  $(1.0-1.2)$  for the 500 nm array, with higher values  $(1.2-1.4)$  for the 440 nm array, and lower values  $(0.7-$   
462  $0.9)$  for the 560 nm array. These values are dependent on field for the 440 nm and 560 nm arrays. Some  
463 uncertainty exists in these values, due to small changes not affecting the patterns generated significantly,  
464 as well as possible errors in tip field estimates.

465  
466

## Appendix C: HIGH APPLIED DC CURRENTS

467 As described on the main text, the application of a DC current leads to a shift (in nm) of the frequency  
468 maps. The shift is attributed to the Lorentz force on the vortices as the current is applied. The forces at  
469 play while the current is applied include the Lorentz force, the pinning force, vortex-vortex interaction  
470 and vortex-field interactions. At low currents, the pinning force counteracts the Lorentz force and the  
471 shift is linear. As the current increases, vortex-vortex and vortex-field interactions likely begin to  
472 dominate and the shift becomes independent of the applied current. At high applied currents, the Lorentz  
473 force is enough to start bulk de-pinning vortices and the frequency map becomes smeared. Fig. 8 shows

474 a set of frequency maps for an array with 500 nm spacing in a 4-vortex configuration at a tip scanning  
475 height of 560 nm. As can be seen from the figure, at a current of 120  $\mu\text{A}$  the frequency map is completely  
476 smeared signaling that the vortices are now fully de-pinned from the array.  
477



478  
479

FIG 8: Frequency maps for a 4-vortex configuration in a 500 nm spaced array at a scanning height of 560 nm with an applied DC current of 0, 40, 60, and 120  $\mu\text{A}$ .

480  
481

## REFERENCES

- 482 1. L. Embon, Y. Anahory, A. Suhov, D. Halbertal, J. Cuppens, A. Yakovenko, A. Uri, Y. Myasoedov,  
483 M. L. Rappaport, M. E. Huber, A. Gurevich, and E. Zeldov, *Probing dynamics and pinning of single*  
484 *vortices in superconductors at nanometer scales*, Sci. Rep. **5**, 7598 (2015).
- 485 2. L. Embon, Y. Anahory, Ž.L. Jelić, E. O. Lachman, Y. Myasoedov, M. E. Huber, G. P. Mikitik, A. V.  
486 Silhanek, M. V. Milošević, A. Gurevich, and E. Zeldov, *Imaging of super-fast dynamics and flow*  
487 *instabilities of superconducting vortices*, Nat. Commun. **8**, 85 (2017).
- 488 3. A. Kremen, S. Wissberg, N. Haham, E. Persky, Y. Frenkel, and B. Kalisky, *Mechanical control of*  
489 *individual superconducting vortices*, Nano Lett. **16**, 1626 (2016).
- 490 4. B. W. Gardner, J. C. Wynn, D. A. Bonn, R. Liang, W. N. Hardy, J. R. Kirtley, V. G. Kogan, and K. A.

- 491 Moler, *Manipulation of single vortices in  $YBa_2Cu_3O_{6.354}$  with a locally applied magnetic field*, Appl.  
492 Phys. Lett. **80**, 1010 (2002).
- 493 5. E. W. J. Straver, J. E. Hoffman, O. M. Auslaender, D. Rugar, and Kathryn A. Moler, *Controlled*  
494 *manipulation of individual vortices in a superconductor*, Appl. Phys. Lett. **93**, 172514 (2008).
- 495 6. J.-Y. Ge, V. N. Gladilin, J. Tempere, C. Xue, J. T. Devreese, J. Van de Vondel, Y. Zhou, and V. V.  
496 Moshchalkov, *Nanoscale assembly of superconducting vortices with scanning tunneling microscope*  
497 *tip*, Nat. Commun. **7**, 13880 (2016).
- 498 7. X. Ma, C. J. O. Reichhardt, and C. Reichhardt, *Manipulation of individual superconducting vortices*  
499 *and stick-slip motion in periodic pinning arrays*, Phys. Rev. B **97**, 214521 (2018).
- 500 8. C.-S. Lee, B. Jankó, I. Derényi & A.-L. Barabási, *Reducing vortex density in superconductors using*  
501 *the 'ratchet effect'*, Nature **400**, 377 (1999).
- 502 9. G. Blatter, M. V. Feigel'man, V. B. Geshkenbein, A. I. Larkin, and V. M. Vinokur, *Vortices in high-*  
503 *temperature superconductors*, Rev. Mod. Phys **66**, 4 (1994).
- 504 10. S. Savel'ev, and F. Nori. *Experimentally realizable devices for controlling the motion of magnetic flux*  
505 *quanta in anisotropic superconductors*, Nat. Mater. **1**, 179 (2002).
- 506 11. V. Vinokur, B. Khaykovich, E. Zeldov, M. Konczykowski, R. A. Doyle, and P. H. Kes. *Lindemann*  
507 *criterion and vortex-matter phase transitions in high-temperature superconductors*, Physica C **295**, 209  
508 (1998).
- 509 12. R. Wördenweber, P. Dymashevski, and V. R. Misko, *Guidance of vortices and the vortex ratchet effect*  
510 *in high- $T_c$  superconducting thin films obtained by arrangement of antidots*, Phys. Rev. B **69**, 184504  
511 (2004).
- 512 13. Y. Togawa, K. Harada, T. Akashi, H. Kasai, T. Matsuda, F. Nori, A. Maeda, and A. Tonomura, *Direct*  
513 *observation of rectified motion of vortices in a niobium superconductor*, Phys. Rev. Lett. **95**, 087002  
514 (2005).
- 515 14. D. Cole, S. Bending, S. Savel'ev, A. Grigorenko, T. Tamegai, and F. Nori, *Ratchet without spatial*  
516 *asymmetry for controlling the motion of magnetic flux quanta using time-asymmetric drives*, Nat.  
517 Mater. **5**, 305 (2006).
- 518 15. X. Ma, C. J. O. Reichhardt, and C. Reichhardt, *Braiding Majorana fermions and creating quantum*  
519 *logic gates with vortices on a periodic pinning structure*, Phys. Rev. B **101**, 024514 (2020).
- 520 16. T. Posske, C.-K. Chiu, and M. Thorwart, *Vortex Majorana braiding in a finite time*, Phys. Rev. Res. **2**,  
521 023205 (2020).
- 522 17. L. N. Vu, M. S. Wistrom, and D. J. Van Harlingen, *Scanning SQUID microscopy of vortex*  
523 *configurations in superconductor arrays*, Physica B **194-196**, 1791 (1994).
- 524 18. A. M. Chang, H. D. Hallen, L. Harriott, H. F. Hess, H. L. Kao, J. Kwo, R. E. Miller, R. Wolfe, and J.

- 525 van der Ziel, *Scanning Hall probe microscopy*, Appl. Phys. Lett. **61**, 1974 (1992).
- 526 19. H. D. Hallen, R. Seshadri, A. M. Chang, R. E. Miller, L. N. Pfeiffer, K. W. West, C. A. Murray, and  
527 H. F. Hess, *Direct spatial imaging of vortices in a superconducting wire network*, Phys. Rev. Lett. **71**,  
528 307 (1993).
- 529 20. H. F. Hess, R. B. Robinson, R. C. Dynes, J. M. Valles, Jr., and J. V. Waszczak, *Scanning-tunneling-*  
530 *microscope observation of the Abrikosov flux lattice and the density of states near and inside a fluxoid*,  
531 Phys. Rev. Lett. **62**, 214 (1989).
- 532 21. L. Thiel, D. Rohner, M. Ganzhorn, P. Appel, E. Neu, B. Müller, R. Kleiner, D. Koelle, and P.  
533 Maletinsky, *Quantitative nanoscale vortex imaging using a cryogenic quantum magnetometer*, Nat.  
534 Nanotechnol. **11**, 677 (2016).
- 535 22. M. Pelliccione, A. Jenkins, P. Ovarthaiyapong, C. Reetz, E. Emmanouilidou, N. Ni, and A. C.  
536 Bleszynski Jayich, *Scanned probe imaging of nanoscale magnetism at cryogenic temperatures with a*  
537 *single-spin quantum sensor*, Nat. Nanotechnol. **11**, 700 (2016).
- 538 23. H. J. Hug, A. Moser, I. Parashikov, B. Stiefel, O. Fritz, H.-J. Güntherodt, and H. Thomas, *Observation*  
539 *and manipulation of vortices in a  $YBa_2Cu_3O_7$  thin film with a low temperature magnetic force*  
540 *microscope*, Physica C **235-240**, 2695 (1994).
- 541 24. O. M. Auslaender, L. Luan, E. W. J. Straver, J. E. Hoffman, N. C. Koshnick, E. Zeldov, D. A. Bonn,  
542 R. Liang, W. N. Hardy, and K. A. Moler, *Mechanics of individual isolated vortices in a cuprate*  
543 *superconductor*, Nat. Phys. **5**, 35 (2009).
- 544 25. L. Bossoni, P. Carretta, and M. Poggio, *Vortex lattice melting of a  $NbSe_2$  single grain probed by*  
545 *ultrasensitive cantilever magnetometry*, Appl. Phys. Lett. **104**, 182601 (2014).
- 546 26. V. V. Dremov, S. Yu. Grebenchuk, A. G. Shishkin, D. S. Baranov, R. A. Hovhannisyan, O. V.  
547 Skryabina, N. Lebedev, I. A. Golovchanskiy, V. I. Chichkov, C. Brun, T. Cren, V. M. Krasnov, A. A.  
548 Golubov, D. Roditchev, and Vasily S. Stolyarov, *Local Josephson vortex generation and manipulation*  
549 *with a magnetic force microscope*, Nat. Comm. **10**, 4009 (2019).
- 550 27. H. Polshyn, T. R. Naibert, and R. Budakian, *Imaging phase slip dynamics in micron-size*  
551 *superconducting rings*, Phys. Rev. B **97**, 184501 (2018).
- 552 28. H. Polshyn, T. Naibert, and R. Budakian, *Manipulating multivortex states in superconducting*  
553 *structures*, Nano. Lett. **19**, 5476 (2019).
- 554 29. M. Tinkham. *Introduction to superconductivity* (Dover, New York, second edition, 2004).
- 555 30. J. R. Phillips, H. S. J. van der Zant, J. White, and T. P. Orlando, *Influence of induced magnetic fields*  
556 *on the static properties of Josephson-junction arrays*, Phys. Rev. B **47**, 5219 (1993).
- 557 31. S. Eley, S. Gopalakrishnan, P. M. Goldbart, and N. Mason, *Approaching zero-temperature metallic*  
558 *states in mesoscopic superconductor-normal-superconductor arrays*, Nat. Phys. **8**, 59 (2012).

- 559 32. T. R. Albrecht, P. Grütter, D. Horne, and D. Rugar, *Frequency modulation detection using high- $Q$*   
560 *cantilevers for enhanced force microscope sensitivity*, J. Appl. Phys. **69**, 668 (1991).
- 561 33. A. M. Campbell, *The interaction distance between flux lines and pinning centres*, J. Phys. C Solid  
562 State Phys. **4**, 3186 (1971).
- 563 34. R. Fazio and G. Schön. Quantum vortex dynamics in Josephson arrays and optical lattices. *Annalen der*  
564 *Physik*, 524(3-4), 2012.
- 565